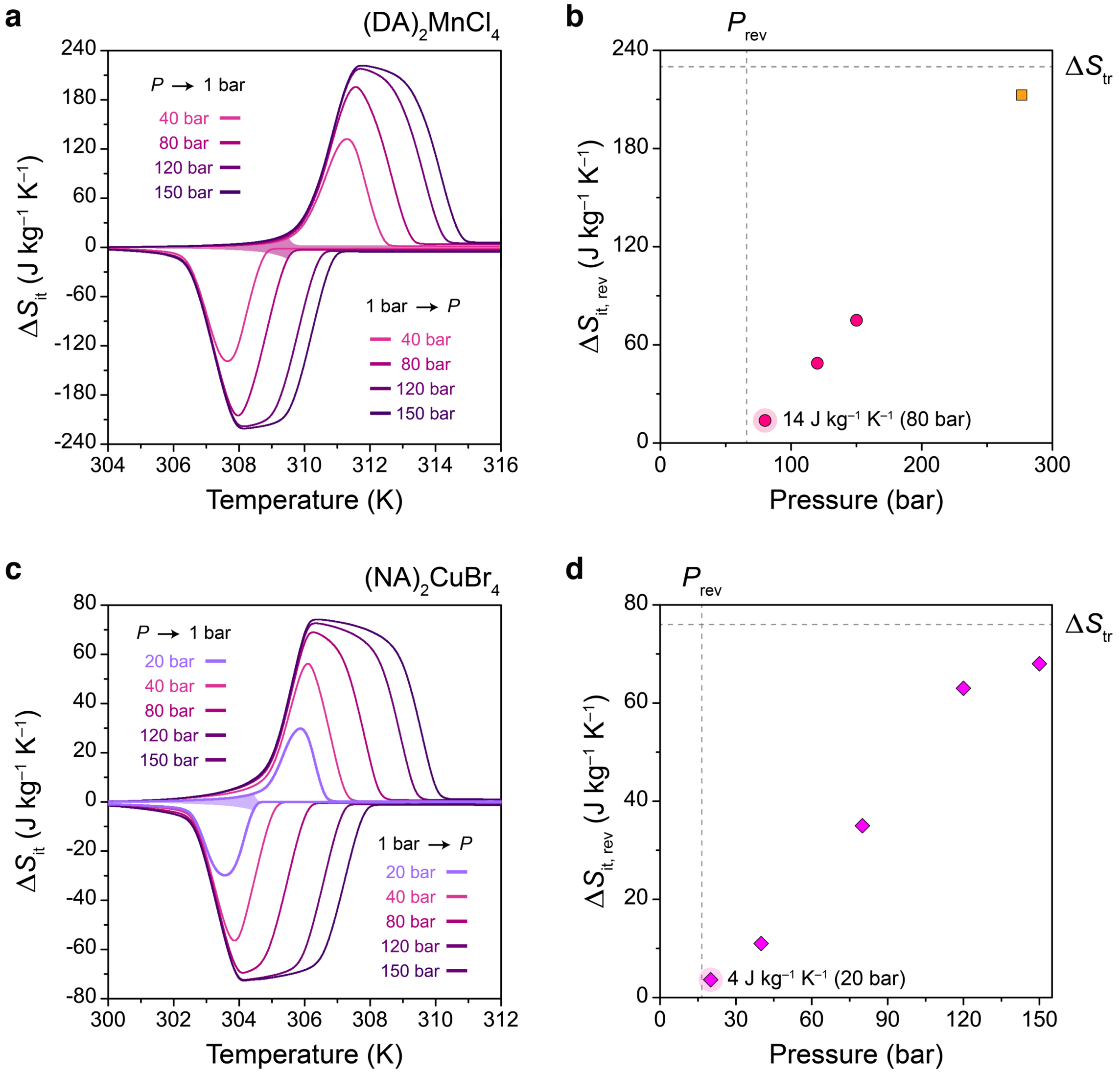

Extended Data Fig. 1 | Reversible isothermal entropy changes. **a**, **c**, Isothermal entropy changes (ΔS_{it}), calculated by the quasi-direct method, for (**a**) $(\mathrm{DA})_2\mathrm{MnCl}_4$ and (**c**) $(\mathrm{NA})_2\mathrm{CuBr}_4$, for compression from ambient pressure and for decompression to ambient pressure. The shaded area indicates the reversible ΔS_{it} within this pressure range. **b**, **d**, Reversible values for ΔS_{it} are shown as a function of pressure for (**b**) $(\mathrm{DA})_2\mathrm{MnCl}_4$ and (**d**) $(\mathrm{NA})_2\mathrm{CuBr}_4$. The minimum pressures required to achieve a reversible entropy change, P_{rev}, are indicated by vertical dashed lines, at 66 bar for $(\mathrm{DA})_2\mathrm{MnCl}_4$ and 16 bar for $(\mathrm{NA})_2\mathrm{CuBr}_4$. For $(\mathrm{DA})_2\mathrm{MnCl}_4$, ΔS_{it} at 280 bar was predicted using a barocaloric coefficient ($\mathrm{d}T_{\mathrm{tr}}/\mathrm{d}P$) of 18.9 K kbar^{-1} (determined by PXRD over the extended pressure range of 1 bar to 360 bar) and using ΔS_{ib} curves obtained at 150 bar under the assumption that ΔS_{ib} curves at 280 bar are similar to those at 150 bar except for a shift in the onset transition temperature.

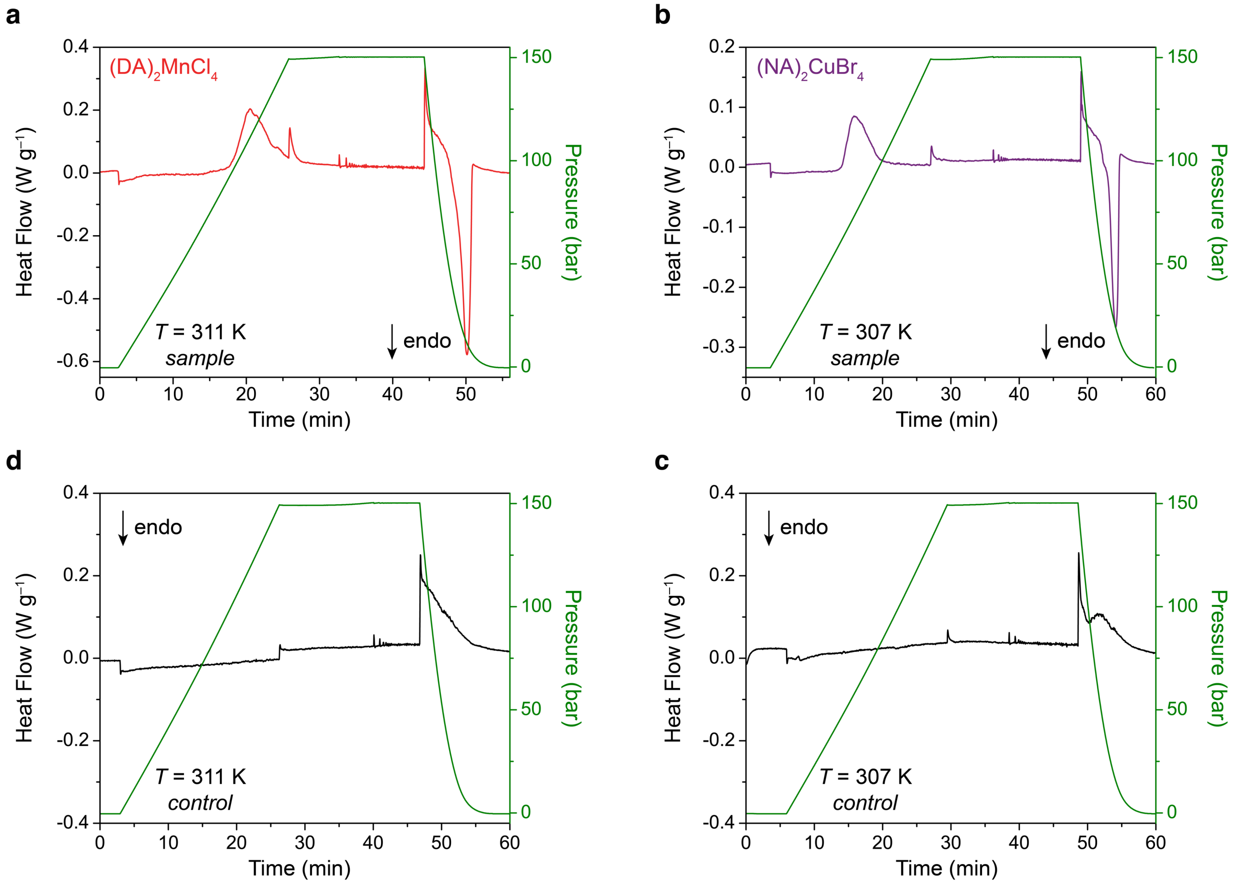

Extended Data Fig. 2 | Quasi-isothermal HP-DSC. a, **b**, Direct evaluation of pressure hysteresis, ΔP_{hys}, through quasi-isothermal DSC experiments for (**a**) $(\mathrm{DA})_2\mathrm{MnCl}_4$ and (**b**) $(\mathrm{NA})_2\mathrm{CuBr}_4$ at 311 K and 307 K, respectively. Heat flow signals were measured as a function of time under the repeated application and removal of a hydrostatic pressure of 150 bar. The pressure was linearly increased at a rate of 6 bar min^{-1} and asymptotically decreased at an average rate of 13 bar min^{-1}. As shown in the raw DSC traces, the application of a hydrostatic pressure induced an exotherm, while the removal of the pressure led to an endotherm. **c**, **d**, In addition to the pressure-induced phase transition, the compression and decompression of the He pressure transmitting medium is also associated with thermal changes that lead to DSC heat signals. While compression led to only small changes in the baseline due to the slow compression rate, the fast decompression from 150 bar induced a sharp exothermic peak as heat flows from the sample into the cooling pressure-transmitting medium. To distinguish the sample heat flows from those associated with He, experiments with a control sample $(\mathrm{C}_{12}\mathrm{H}_{25}\mathrm{NH}_3)_2\mathrm{MnCl}_4$ that does not undergo any phase transitions until above 330 K, well above the transition temperatures for $(\mathrm{DA})_2\mathrm{MnCl}_4$ and $(\mathrm{NA})_2\mathrm{CuBr}_4$, were carried out at (**c**) 311 K and (**d**) 307 K. From these control experiments, the baseline features associated with He compression and decompression were modeled and subtracted from the raw DSC traces, yielding the baseline-corrected DSC traces for $(\mathrm{DA})_2\mathrm{MnCl}_4$ and $(\mathrm{NA})_2\mathrm{CuBr}_4$ shown in Figs. 3c and 3f, respectively.

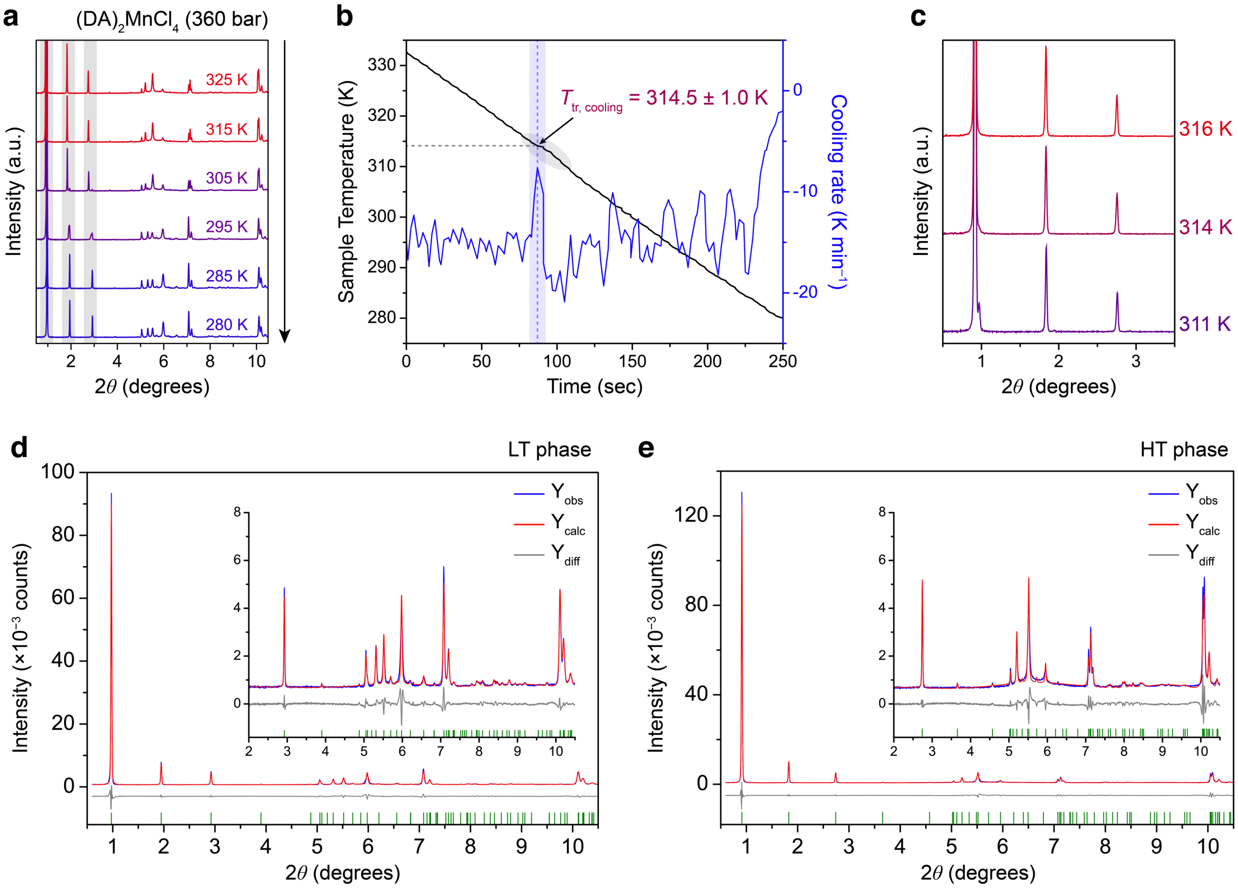

Extended Data Fig. 3 | Chain-melting transition of (DA)$_2$MnCl$_4$ at 360 bar. a, Variable-temperature PXRD for (DA)$_2$MnCl$_4$ at 360 bar while cooling from 335 K to 275 K with an X-ray wavelength of 0.45237 Å. The red and blue patterns correspond to the high-temperature (HT) and low-temperature (LT) phases, respectively, with purple indicating patterns in which both phases are present during the transition from the HT to LT phase. **b**, A sample temperature trace recorded from a thermocouple embedded in the sample capillary is shown (black line), along with the recorded cooling rate (blue line). Note that the thermocouple temperature trace features a peak, which is attributed to the latent heat of the exothermic transition. The transition temperature, T_{tr}, was determined using the first maximum of the cooling rate curve, and the uncertainty of the measurement was estimated as the full width at half maximum of the cooling rate peak. **c**, The phase transition from the HT to LT phase at T_{tr} was identified by monitoring the high-intensity (00*l*) peaks in the low-angle region, where the emergence of a higher-angle shoulder on the right side of each peak is associated with the emergence of the smaller unit cell of the LT phase. **d**, **e**, Le Bail refinements are shown for the (**d**) HT phase (330 K), $R_{\text{wp}} = 7.30\%$, $R_{\text{p}} = 5.23\%$ and (**e**) LT phase (280 K), $R_{\text{wp}} = 7.62\%$, $R_{\text{p}} = 4.91\%$. Blue and red lines correspond to the observed and calculated diffraction patterns, respectively. The grey line represents the difference between observed and calculated patterns, and the green tick marks indicate calculated Bragg peak positions based on the refined unit cell. Unit cell parameters are listed in Supplementary Table 8.

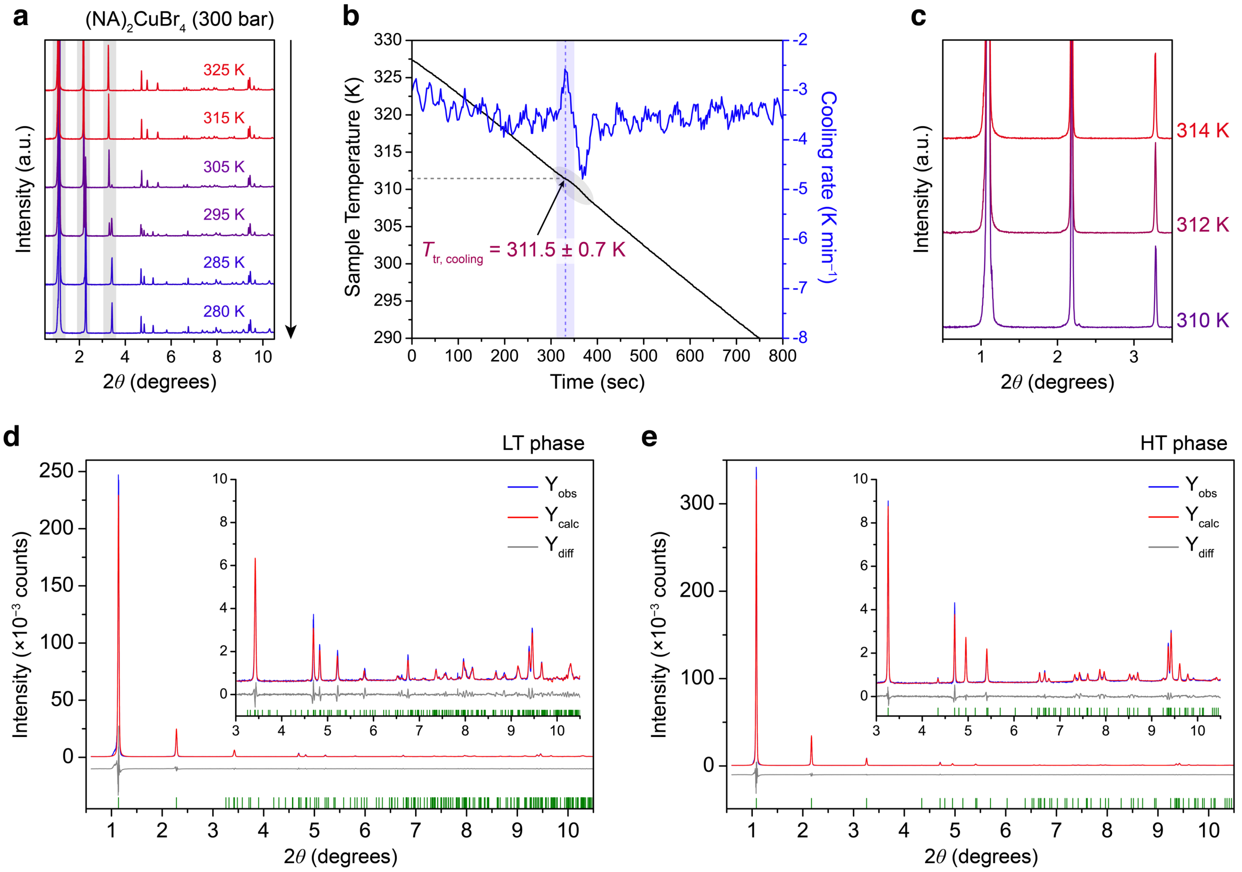

Extended Data Fig. 4 | Chain-melting transition of (NA)$_2$CuBr$_4$ at 300 bar. a, Variable-temperature PXRD for (NA)$_2$CuBr$_4$ at 300 bar while cooling from 335 K to 275 K with an X-ray wavelength of 0.45237 Å. The red and blue patterns correspond to the HT and LT phases, respectively, with purple indicating patterns in which both phases are present during the transition from the HT to LT phase. **b**, A sample temperature trace recorded from a thermocouple embedded in the sample capillary is shown (black line), along with the recorded cooling rate (blue line). Note that the thermocouple temperature trace features a peak, which is attributed to the latent heat of the exothermic transition. The transition temperature, T_{tr}, was determined using the first maximum of the cooling rate curve, and the uncertainty of the measurement was estimated as the full width at half maximum of the cooling rate peak. **c**, The phase transition from the HT to LT phase at T_{tr} was identified by monitoring the high-intensity (00*l*) peaks in the low-angle region, where the emergence of a higher-angle shoulder on the right side of each peak is associated with the emergence of the smaller unit cell of the LT phase. **d**, **e**, Le Bail refinements are shown for the (**d**) HT phase (314 K), R_{wp} = 8.33%, R_{p} = 5.38% and (**e**) LT phase (280 K), R_{wp} = 14.7%, R_{p} = 9.29%. Blue and red lines correspond to the observed and calculated diffraction patterns, respectively. The grey line represents the difference between observed and calculated patterns, and the green tick marks indicate calculated Bragg peak positions based on the refined unit cell. Unit cell parameters are listed in Supplementary Table 9.

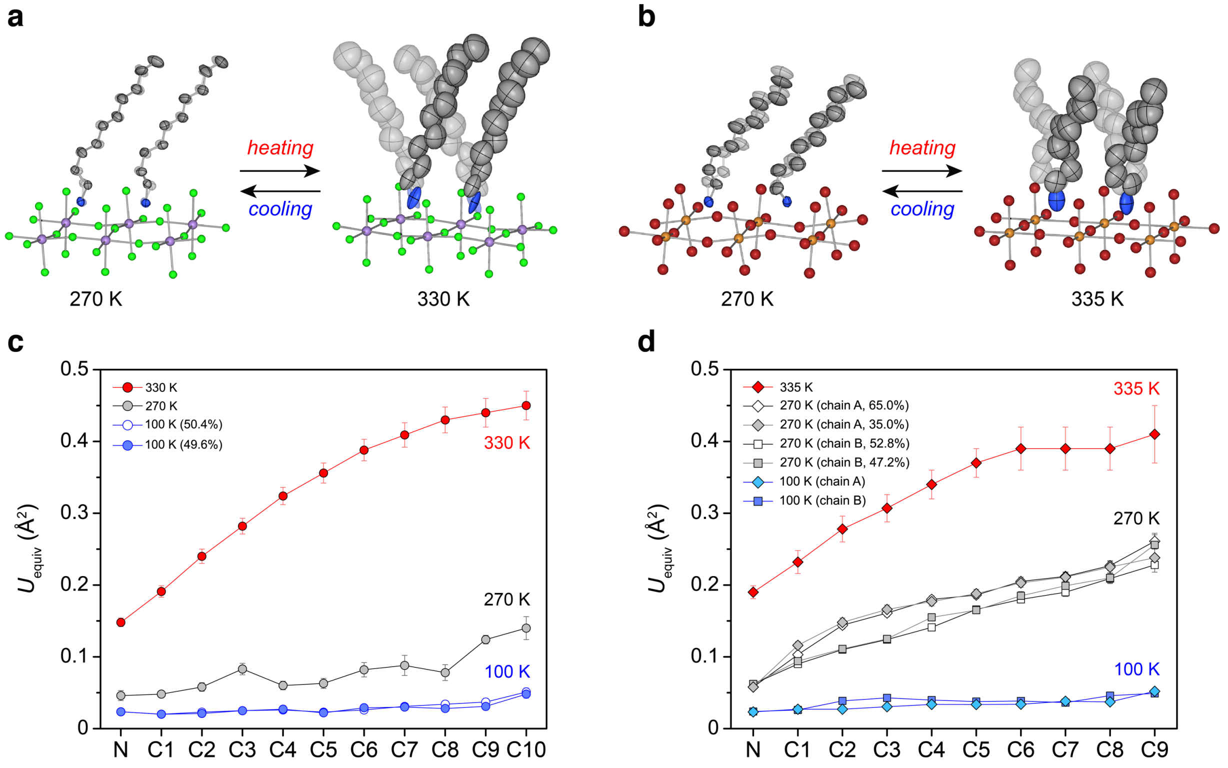

Extended Data Fig. 5 | Variable-temperature single-crystal structures. **a**, **b**, Conformations of the alkylammonium chains in the LT and HT phases of (**a**) $(DA)_2MnCl_4$ and (**b**) $(NA)_2CuBr_4$, with atomic displacement parameters shown at 50% probability for the C and N atoms of the alkylammonium chains. In the LT phase, decylammonium (DA) chains in $(DA)_2MnCl_4$ display one conformation, with a single gauche C–C bond (C2–C3), while nonylammonium (NA) chains in $(NA)_2CuBr_4$ adopt two conformations, alternating between chains with a gauche C1–C2 bond (chain A) and those with a gauche C2–C3 bond (chain B). Purple, orange, green, brown, grey, and blue spheres represent Mn, Cu, Cl, Br, C, and N atoms, respectively. H atoms are omitted for clarity. Note that DA chains are disordered over a special position in both the LT and HT phases, while NA chains are modeled with two-part disorder in the LT phase and disordered over a special position in the HT phase. **c**, **d**, Temperature dependence of U_{equiv} (equivalent isotropic displacement parameters) is shown for (**c**) $(DA)_2MnCl_4$ and (**d**) $(NA)_2CuBr_4$, at 100 K, 270 K (LT phase), and 330/335 K (HT phase).

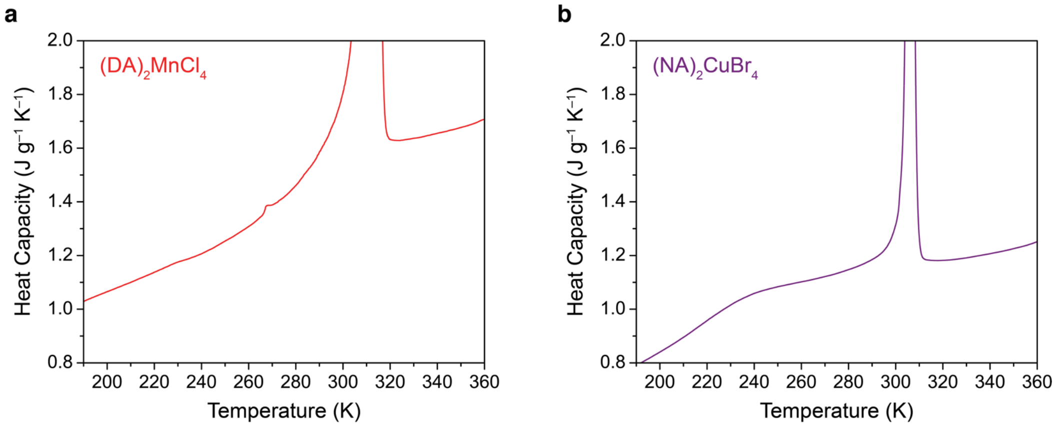

Extended Data Fig. 6 | Heat capacity. a, **b**, Temperature dependence of specific heat capacity for (**a**) $(DA)_2MnCl_4$ and (**b**) $(NA)_2CuBr_4$ obtained from heating with a scan rate of 10 K min^{-1} from 190 to 360 K. The data shown represents one three-run ASTM heat capacity set, with no averaging. In contrast to $(DA)_2MnCl_4$, $(NA)_2CuBr_4$ displays a broad feature from 220–250 K, which is consistent with the gradual activation of conformational degrees of freedom prior to the chain-melting transition.

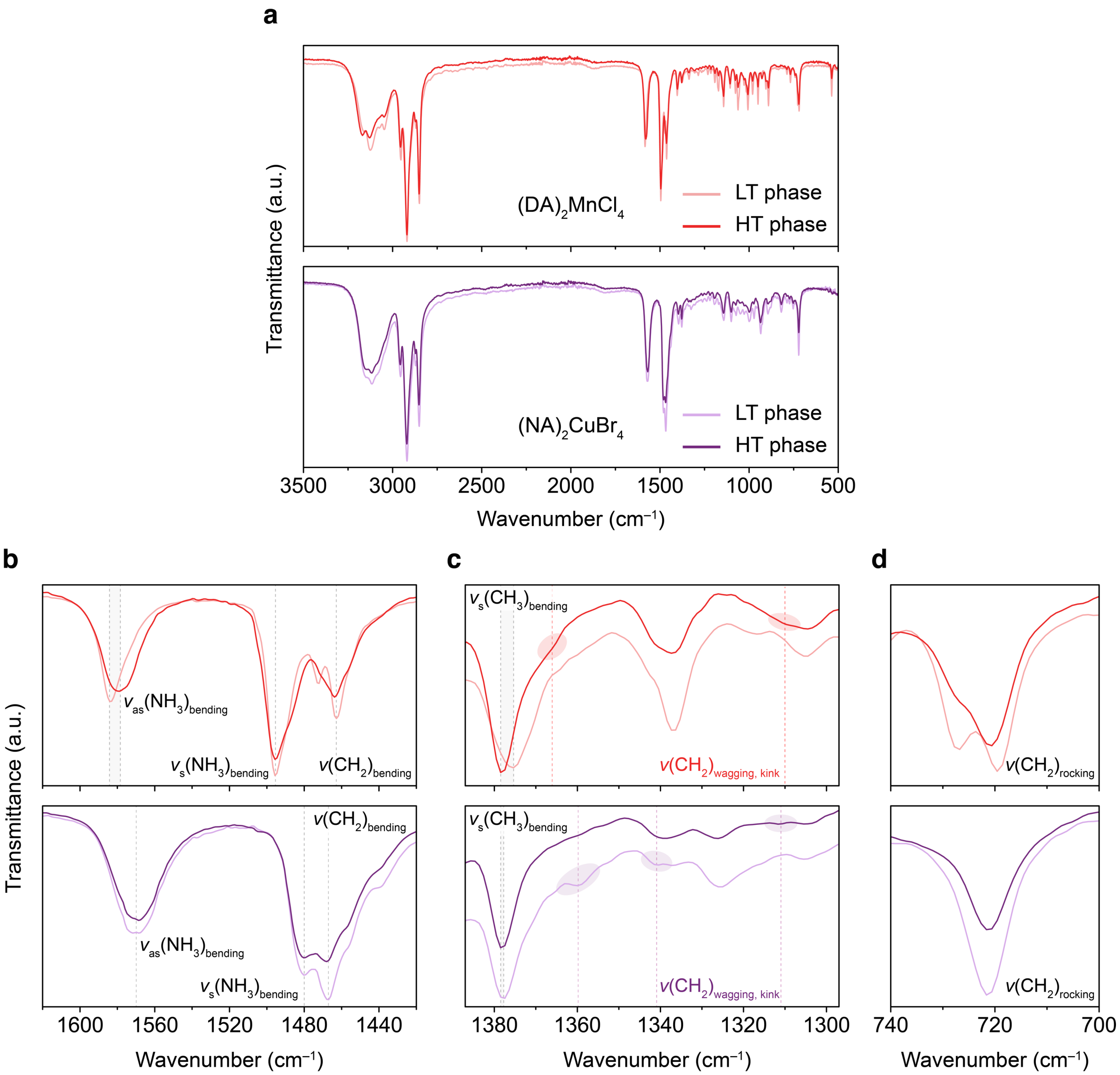

Extended Data Fig. 7 | Variable-temperature infrared spectra. a, The LT and HT phase spectra were collected 5 K below and 5 K above the phase transition temperature, respectively, for $(DA)_2MnCl_4$ (top, red traces) and $(NA)_2CuBr_4$ (bottom, purple traces). **b**–**d**, Zoomed in views of three different regions with bands that correspond to (**b**) NH_3 bending and CH_2 bending, (**c**) CH_3 bending and CH_2 wagging, and (**d**) CH_2 rocking bands. Key shifts in peak positions are indicated by dashed lines, and CH_2 wagging bands associated with conformational defects are highlighted with red and purple dashed lines for $(DA)_2MnCl_4$ and $(NA)_2CuBr_4$, respectively. Note that previous reports on $(C_nH_{2n+1}NH_3)_2MCl_4$ (M = Cd, Mn) perovskites revealed that the peak near 1337 cm^{-1} does not depend on chain conformation[41,42]. The IR bands used for conformational analysis are summarized in Supplementary Table 5.

Extended Data Table 1 | Phase-change properties and barocaloric effects of representative barocaloric materials shown in Fig. 4.

Type	Chemical Formula[a]	T_{tr}[b]	ΔS_{tr}[c] (J kg^{-1} K^{-1})	dT_{tr}/dP *heating* (K kbar^{-1})	dT_{tr}/dP *cooling* (K kbar^{-1})	ΔT_{hys}[d] (K)	P_{rev}[e] (bar)	$\Delta S_{it,rev}$[f] (J kg^{-1} K^{-1})	ΔP[f] (bar)	Ref.
2-D perovskites	$(DA)_2MnCl_4$	310	230	22.1 (29)[g]	20.6	1.4	66	75 (210)[h]	150 (280)[h]	this work
	$(NA)_2CuBr_4$	305	76	26.9 (33)[g]	26.5	0.4	16	68	150	
3-D hybrid perovskites	$[(CH_3)_4N][Mn(N_3)_3]$	305	80	12[i]		7	583	70	900	[43]
	[TPrA][Mn(dca)$_3$]	330	43	23.1[i]		0.9	39	31	70	[44]
	[TPrA][Cd(dca)$_3$]	386	16	38.2[i]		1.4	37	11.5	70	[45]
Organic plastic crystals	$(CH_3)_2C(CH_2OH)_2$	314	389	11.3	9.3	14	1505	445	2500	[10, 11]
	$(CH_3)C(CH_2OH)_3$	354	485	7.9	9.4	3.7	394	490	2400	[9]
	$(CH_3)_3C(CH_2OH)$	232	204	22	11.9	20.3	1706	290	2600	[9]
	C_{60}	259	27	16.7	17.2	3	174	32 (42)	1000 (4100)	[46]
Inorganic salts	$(NH_4)_2SO_4$	222	65	–5.7	–4.5	1	175	60	1000	[39]
	AgI	420	64	–14	–12.8	25	1786	60	1000	[47]
	$Ni_{0.85}Fe_{0.15}S$[j]	303	53	–7.5		11.5	1533			[48]
Alloys	$Fe_{49}Rh_{51}$	310	13	5.4	6.4	10	1563	13	2500	[49]
	$Ni_{50}Mn_{31.5}Ti_{18.5}$	255	85	1.9	3.2	12	3750	35	3800	[50]
Spin-crossover complexes	$Fe_3(bntrz)_6(tcnset)_6$	318	80	25	25	2	80	80 (120)	550 (2600)	[51]
	$[FeL_2](BF_4)_2$[j]	262	86	10[k]	10[k]	4	400			[52]

[a] DA = decylammonium; NA = nonylammonium; TPrA = tetrapropylammonium; bntrz = 4-(benzyl)-1,2,4-triazole; tcnset = 1,1,3,3-tetracyano-2-thioethylepropenide; L = 2,6-di(pyrazol-1-yl)pyridine. [b] Transition temperatures measured during heating are tabulated here. [c] Entropies of transitions measured at ambient pressure are tabulated here. [d] $\Delta T_{hys} = T_{tr,\ heating} - T_{tr,\ cooling}$ at ambient pressure. [e] Calculated using $P_{rev} = \Delta T_{hys} / |dT_{tr}/dP|$, with d$T_{tr}$/d$P$ values for exothermic and endothermic transitions used for normal and inverse barocaloric materials, respectively. Note that inverse barocaloric materials refer to compounds with dT_{tr}/dP < 0. [f] Reversible isothermal entropy changes, $\Delta S_{it,\ rev}$, at the driving pressure ΔP are tabulated here. Note that these values were derived from quasi-direct measurements[6,26]. At high pressures (typically above 1 kbar), the additional entropy changes outside of the transition, ΔS_{+}, contribute to ΔS_{it} values, leading to ΔS_{it} values that can exceed ΔS_{tr}. [g] Calculated from the Clausius–Clapeyron equation ($dT_{tr}/dP = \Delta V_{tr}/\Delta S_{tr}$). [h] By assuming that the isobaric entropy curves at 280 bar are similar to those at 150 bar except for a shift in the onset transition temperature, $\Delta S_{it,\ rev}$ at 280 bar was predicted using the barocaloric coefficient of 18.9 K kbar^{-1} as determined from PXRD over the extended pressure range of 1 bar to 360 bar (Extended Data Fig. 1). [i] dT_{tr}/dP values were averaged from heating and cooling data. [j] Only an irreversible ΔS_{it} value is reported ($Ni_{0.85}Fe_{0.15}S$, 53 J kg^{-1} K^{-1} at 1000 bar; $[FeL_2](BF_4)_2$, 68 J kg^{-1} K^{-1} at 430 bar). [k] dT_{tr}/dP values obtained at a pressure range < 2 kbar values are shown, with $(dT_{tr}/dP)_{heating}$ and $(dT_{tr}/dP)_{cooling}$ obtained from calorimetry and SQUID magnetometry, respectively.

Extended Data Table 2 | Barocaloric strengths and predicted thermodynamic efficiencies for selected barocaloric materials.

Chemical Formula[a]	T_{tr}[b]	$\Delta S_{\mathrm{it,\,rev}} / \Delta P$[c] (J kg^{-1} K^{-1} kbar^{-1})	$\Delta T_{\mathrm{ad,\,max}}$[d] (K)	$\Delta T_{\mathrm{hys}} / \Delta T_{\mathrm{ad,max}}$[e] (%)	η[f] (%)	**Ref.**
$(\mathrm{DA})_2\mathrm{MnCl}_4$	310	500	43[g]	3.3	89	this work
$(\mathrm{NA})_2\mathrm{CuBr}_4$	305	453	18[h]	2.2	92	
$[\mathrm{TPrA}][\mathrm{Mn(dca)}_3]$	330	436	5[i]	15.8	61	[44]
$(\mathrm{CH}_3)_2\mathrm{C}(\mathrm{CH}_2\mathrm{OH})_2$	314	178	45[j]	31.1	45	[10, 11]
C_{60}	259	32	20[k]	15.0	63	[46]
$(\mathrm{NH}_4)_2\mathrm{SO}_4$	222	60	8[l]	12.5	67	[39]
$\mathrm{Ni}_{0.85}\mathrm{Fe}_{0.15}\mathrm{S}$	303		30[m]	38.3	40	[48]
$\mathrm{Fe}_3(\mathrm{bntrz})_6(\mathrm{tcnset})_6$	318	145	35[n]	5.7	81	[51]

[a] DA = decylammonium; NA = nonylammonium; TPrA = tetrapropylammonium; bntrz = 4-(benzyl)-1,2,4-triazole; tcnset = 1,1,3,3-tetracyano-2-thioethylepropenide. [b] Transition temperatures measured during heating are tabulated here. [c] The reversible isothermal entropy change $\Delta S_{\mathrm{it,rev}}$ normalized by the driving pressure is often referred to as barocaloric strength and can provide a useful way of comparing barocaloric effects across different materials[26]. For consistency and due to limitations of available data from previous reports, the barocaloric strength values for all compounds were determined by choosing the smallest ΔP values that capture the maximum entropy of the transition. [d] Maximum adiabatic temperature changes tabulated here were calculated using the indirect method, with $\Delta T_{\mathrm{ad,max}} = T\Delta S_{\mathrm{it}} / c_{\mathrm{p}}$, or, by quasi-direct methods[26]. [e] ΔT_{hys} values measured at ambient pressure were used for the calculation. [f] The second-law efficiency, η, which corresponds to the coefficient of performance (COP) of material with hysteresis normalized by COP for a Carnot cycle ($\mathrm{COP}_{\mathrm{Carnot}}$), is estimated using the equation $\eta = \mathrm{COP}/\mathrm{COP}_{\mathrm{Carnot}} = \frac{1}{1+4\frac{\Delta T_{\mathrm{hys}}}{\Delta T_{\mathrm{ad,\,max}}}}$ (ref. 14). Note that this relation is derived from a phenomenological model that integrates the dissipative losses due to hysteresis in a Carnot-like cycle and offers insight into how the thermal hysteresis of a material impacts efficiency. [g] Estimated using the indirect method, with $\Delta S_{\mathrm{it,rev}}$ of 213 J kg^{-1} K^{-1} predicted to occur at the driving pressure of 280 bar with $T = 312$ K and $c_{\mathrm{p}} = 1550$ J kg^{-1} K^{-1} (Extended Data Fig. 1). [h] Estimated using the indirect method, with $\Delta S_{\mathrm{it,\,rev}}$ of 68 J kg^{-1} K^{-1} from the pressure change of 150 bar with $T = 306$ K and $c_{\mathrm{p}} = 1180$ J kg^{-1} K^{-1} (Extended Data Fig. 1). [i] Estimated using the indirect method, with $\Delta S_{\mathrm{it,\,rev}}$ of 35 J kg^{-1} K^{-1} from a pressure change of 69 bar with $T = 332$ K and $c_{\mathrm{p}} = 2450$ J kg^{-1} K^{-1}. [j] Quasi-direct measurements at a driving pressure of 5700 bar (ref. 11). [k] Quasi-direct measurements at a driving pressure of 5900 bar. [l] Estimated using the indirect method, with $\Delta S_{\mathrm{it,\,rev}}$ of 60 J kg^{-1} K^{-1} at a driving pressure of 1000 bar with $c_{\mathrm{p}} = 1700$ J kg^{-1} K^{-1}. [m] Estimated using the indirect method, with the irreversible ΔS_{it} value of 53 J kg^{-1} K^{-1} at a driving pressure of 1000 bar. [n] Quasi-direct measurements at a driving pressure of 2600 bar.